https://doi.org/10.5194/egusphere-2023-316
Preprint. Discussion started: 13 March 2023

A linear assessment of waveguidability for barotropic Rossby waves in different large-scale flow configurations

Antonio Segalini[1], Jacopo Riboldi[1], Volkmar Wirth[2], and Gabriele Messori[1,3,4,5]

[1]Department of Earth Sciences, Uppsala University, Villavägen 16, 752 36 Uppsala, Sweden
[2]Institute for Atmospheric Physics, Johannes Gutenberg University Mainz, Becherweg 21, 55128 Mainz, Germany
[3]Centre of Natural Hazards and Disaster Science (CNDS), Uppsala University, Villavägen 16, 75236 Uppsala, Sweden
[4]Department of Meteorology, Stockholm University, Svante Arrhenius väg 16c, 114 18 Stockholm, Sweden
[5]Bolin Centre for Climate Research, Stockholm University, Svante Arrhenius väg 8, 114 18 Stockholm, Sweden

Correspondence: Antonio Segalini (antonio.segalini@geo.uu.se)

Abstract. Topographically forced Rossby waves shape the upper-level waveguide over the midlatitudes, affecting the propagation of transient waves therein, and have been linked to multiple surface extremes. The complex interplay between the forcing and the background flow in shaping the Rossby wave response still needs to be elucidated in a variety of configurations. We propose here an analytical solution of the linearized barotropic vorticity equation to obtain the stationary forced Rossby wave resulting from arbitrary combinations of forcing and background zonal wind. While the onset of barotropic instability might hinder the applicability of the linear framework, we show that the nonlinear wave response can still be retrieved qualitatively from the linearized solution. Examples using single- and double-jet configurations are discussed to illustrate the method and study how the background flow can act as a waveguide for Rossby waves.

1 Introduction

Rossby waves are a fundamental component of the upper-tropospheric dynamics (Rossby, 1939, 1940) and are instrumental in modulating the location, intensity, and track of extratropical weather systems. They owe their existence and characteristics to the rotation of the Earth and its spherical geometry. A key characteristic of Rossby waves, which has profound implications for their modulation of weather systems, is their propagation. The Earth's roughly spherical geometry usually leads to the equatorward refraction of Rossby waves (Hoskins and Karoly, 1981), yet the presence of localised upper tropospheric jet streams can favour a zonal propagation (e.g., Hoskins and Valdes, 1990; Ambrizzi et al., 1995; Branstator, 2002; Wirth et al., 2018). The capability of jet streams to promote Rossby wave propagation, referred to as "waveguidability", has long been object of research (see the reviews by Wirth et al., 2018; White et al., 2022). Waveguides typically exist for time scales longer than the waves they "guide", and this property can be exploited to understand persistence and predictability of midlatitude weather (Martius et al., 2010). The amplification and propagation of Rossby waves along such waveguides has been related in the literature to the occurrence of extreme weather events both in winter (e.g., Davies, 2015; Harnik et al., 2016) and summer (e.g., Kornhuber et al., 2019; Teng and Branstator, 2019; Di Capua et al., 2021; Rousi et al., 2022; Jiménez-Esteve et al., 2022). In a number of these examples, the Rossby waves were identified as quasi-stationary and associated with concurrent extremes in geographically remote regions due to the zonally-extended, large-amplitude nature of the waves. The existence of quasi-stationary waves on a mid-latitude waveguide has also been linked to the phenomenon of quasi-resonance, namely a constructive self-interference of the wave, which in turn may be linked to surface extreme events (Petoukhov et al., 2013; Coumou et al., 2014); however, whether or not quasi-resonance is a relevant mechanism in realistic situations is an unsolved question (Wirth and Polster, 2021). In a longer term perspective, anthropogenic global warming can modify the position and strength of extratropical waveguides, thus systematically affecting the amplitude and the propagation of Rossby waves and the persistence of the associated weather systems (as discussed by Hoskins and Woollings, 2015).

The relevance that waveguidability plays in atmospheric dynamics, as well as its connection to surface extremes in a changing climate, has led to a renewed interest in its study (White et al., 2022). In general, waveguidability is regarded as a property of the background flow configuration in which Rossby waves are propagating. Which properties such a background flow should have to enable strong waveguidability is a complex issue, in particular when using real-world observations (e.g., to study the role played by Rossby waveguides in extreme weather events). Indeed, the very existence of a waveguide critically depends on the characteristics of the background state (Held et al., 2002; Wirth and Polster, 2021). Temporal filtering or moving time averages of upper-level winds have been widely used to estimate the background flow in which transient Rossby waves propagate (e.g., Branstator, 2002; Stadtherr et al., 2016; Petoukhov et al., 2016; Kornhuber et al., 2017), but this approach has several drawbacks. First of all, it can filter out propagating waves and overemphasize the role played by quasi-stationary Rossby waves (as dicussed by Fragkoulidis et al., 2018; Riboldi et al., 2022). Perhaps more critically, this approach relies on the assumption that a clear separation exists between the propagating waves and their waveguide, such that the former are not leaving their signature on the latter. However, this assumption is violated when Rossby waves reach significant meridional amplitudes, as often happens in the context of large-scale flow configurations associated with unusual or extreme weather (Wirth and Polster, 2021).

The role of specific background flow configurations in promoting waveguidability can be investigated in detail using idealized frameworks. Manola et al. (2013) and Wirth (2020) are notable examples of such work for the cases of single, localised jet streams in the Northern Hemisphere. These studies noticed that waveguidability increases with the strength of the jet and that latitudinally narrow jets are more efficient waveguides than broad jets. However, there is a lack of understanding of the implications of other background flow configurations, such as the presence of two separate jet streams, which has been linked to summertime heatwaves (“double jets”; e.g., Coumou et al., 2014; Rousi et al., 2022).

Studying waveguidability requires, indeed, a systematical investigation of a large number of different background flows. Each flow case must also be investigated for different forcings to assess the flow response. This quickly becomes demanding in terms of computational resources and expert analysis time. A possible way to overcome these limitations is the development of an analytical framework to study Rossby waves dynamics and their waveguidability, thus avoiding numerical integration of the underlying equations. Similar approaches have been previously employed to study other types of oscillatory phenomena, such as Rossby wave critical layers (Campbell and Maslowe, 1998), equatorial waves (Boyd, 1978) and gravity waves (Baldauf and Brdar, 2013).

https://doi.org/10.5194/egusphere-2023-316
Preprint. Discussion started: 13 March 2023

In this work, we propose an analytical framework to study waveguidability by solving *explicitly* the linearized, 2-D barotropic vorticity equation in terms of normal mode analysis. This enables one to inexpensively obtain analytical solutions for in principle any forcing under a given background flow, thus allowing to study waveguidability in greater detail. We validate the solutions by comparing them with the output of nonlinear numerical simulations based on a spectral code built on spherical harmonics. The joint analysis of linear and nonlinear solutions further allows a detailed investigation of the stability of different wave modes. The paper is structured as follows: section 2 presents the theory behind the linear approach, while its discrete implementation based on orthogonal Chebyshev polynomials is discussed in the paper appendix. A comparison between linear and nonlinear calculations is discussed in section 3 where different zonal wind profiles are investigated in terms of both the wave spatial structure and of integrated parameters such as the waveguidability. The time evolution of the simulation is also discussed up to the point where the linear simulation becomes unstable. The stability analysis for a single-jet configuration and remarks about waveguidability in a double-jet configuration are discussed respectively in section 4.3 and 5. The paper is closed by some concluding remarks in section 6.

2 Analytical model and numerical details

Let us consider the two-dimensional barotropic vorticity equation on a spherical planet with radius a^* (in this section dimensional quantities are indicated by means of an asterisk superscript)

$$\frac{\partial \zeta^*}{\partial t^*} + (\mathbf{V}^* \cdot \nabla_h)(\zeta^* + f^*) = -\lambda_r^* (\zeta^* - \zeta_0^*) + F^*, \tag{1}$$

where $\mathbf{V}^*$ is the horizontal velocity field, $f^* = 2\Omega^* \cos\theta$ is the Coriolis parameter, $\theta = \pi/2 - \varphi$ is the colatitude (associated with the latitude φ) and λ is the longitude. Similarly to Wirth (2020), λ_r^* indicates the damping rate, ζ_0^* the background flow vorticity and F^* a generic forcing in space and time. By normalising physical quantities with respect to the planet radius a^* and a characteristic velocity U_s^* such that

$$t = \frac{t^*}{a^*/U_s^*} \quad , \quad \mathbf{V} = \frac{\mathbf{V}^*}{U_s^*} \quad , \quad \zeta = \frac{\zeta^*}{U_s^*/a^*} \quad , \quad f = \frac{f^*}{2\Omega^*} = \cos\theta \quad , \quad F = \frac{F^*}{(U_s^*/a^*)^2}, \tag{2}$$

the barotropic vorticity equation (1) is re-written in dimensionless form as

$$\frac{\partial \zeta}{\partial t} + (\mathbf{V} \cdot \nabla_h)\left(\zeta + \frac{f}{\mathrm{Ro}}\right) = -\lambda_r (\zeta - \zeta_0) + F \qquad \text{with} \qquad \mathrm{Ro} = \frac{U_s^*}{2\Omega^* a^*}. \tag{3}$$

The choice of the characteristic velocity scale, U_s^*, is arbitrary but it should be of the same order of magnitude of the velocity field. In the considered two-dimensional case, the flow divergence is zero everywhere so that a streamfunction, Ψ, can be introduced, facilitating the determination of the velocity and vorticity fields as

$$u_\theta = -\frac{1}{\sin\theta}\frac{\partial \Psi}{\partial \lambda} \quad , \quad u_\lambda = \frac{\partial \Psi}{\partial \theta} \quad , \quad \zeta = \nabla^2 \Psi. \tag{4}$$

By assuming a base zonal flow $u_\lambda = U(\theta)$ and $u_\theta = 0$, the undisturbed vorticity, ζ_0, is given by

$$\zeta_0(\theta) = \frac{1}{\sin\theta}\frac{\partial}{\partial \theta}(U \sin\theta) = \cot\theta\, U + \frac{\partial U}{\partial \theta} \qquad \text{for} \qquad 0 < \theta < \pi, \tag{5}$$

while at the poles no singularity of (5) is present if $U(0) = U(\pi) = 0$ so that

$$\zeta_0(0) = 2\left.\frac{\partial U}{\partial \theta}\right|_{\theta=0} \qquad , \qquad \zeta_0(\pi) = 2\left.\frac{\partial U}{\partial \theta}\right|_{\theta=\pi} . \tag{6}$$

Let us consider a perturbed problem where the relative vorticity is given by $\zeta = \zeta_0 + \zeta'$. This will be associated with a streamfunction, $\Psi_0 + \psi'$, and velocity field

$$\mathbf{V} = (u_\theta, u_\lambda) = (0, U) + (u'_\theta, u'_\lambda) = (0, U) + \left(-\frac{1}{\sin\theta}\frac{\partial \psi'}{\partial \lambda}, \frac{\partial \psi'}{\partial \theta}\right) . \tag{7}$$

The equation governing the small perturbation is obtained by taking (3) and subtracting the base-state equation. By neglecting the nonlinear terms (small for infinitesimal perturbations), one obtains the linearised barotropic vorticity equation

$$\frac{\partial \zeta'}{\partial t} + \frac{U}{\sin\theta}\frac{\partial \zeta'}{\partial \lambda} + u'_\theta \frac{\partial}{\partial \theta}\left(\zeta_0 + \frac{f}{\mathrm{Ro}}\right) = -\lambda_r \zeta' + F , \tag{8}$$

with

$$\zeta' = \nabla_h^2 \psi' \qquad , \qquad u'_\theta = -\frac{1}{\sin\theta}\frac{\partial \psi'}{\partial \lambda} . \tag{9}$$

The system can be better analysed by taking the Fourier transform in the zonal direction (with wavenumber m) leading to

$$\frac{\partial \widehat{\zeta}}{\partial t} + \left(\frac{imU}{\sin\theta} + \lambda_r\right)\widehat{\zeta} + \widehat{u_\theta}\frac{\partial}{\partial \theta}\left(\zeta_0 + \frac{f}{\mathrm{Ro}}\right) = \widehat{F} , \tag{10}$$

where

$$\widehat{\zeta} = \frac{\partial^2 \widehat{\psi}}{\partial \theta^2} + \cot\theta \frac{\partial \widehat{\psi}}{\partial \theta} - \frac{m^2}{\sin^2\theta}\widehat{\psi} = \mathcal{L}\widehat{\psi} \qquad , \qquad \widehat{u_\theta} = -\frac{im}{\sin\theta}\widehat{\psi} , \tag{11}$$

where $\mathcal{L}$ indicates the Laplace operator that, once discretised, becomes a numerical matrix. By introducing the matrix $B = i\mathcal{L}$ and the streamfunction vector $\widehat{\psi}_j = \widehat{\psi}(\theta_j; m)$ evaluated at the colatitudes θ_j, the barotropic vorticity equation (10) is written as

$$-iB\frac{\partial \widehat{\psi}_j}{\partial t} + \left[\left(\frac{imU}{\sin\theta} + \lambda_r\right)\mathcal{L} - \frac{im}{\sin\theta}\frac{\partial}{\partial \theta}\left(\zeta_0 + \frac{f}{\mathrm{Ro}}\right) I\right]\widehat{\psi}_j = -iB\frac{\partial \widehat{\psi}_j}{\partial t} + A\widehat{\psi}_j = \widehat{F} , \tag{12}$$

where the terms composing the matrix A are grouped within the square brackets in (12) and I is the identity matrix (see appendix A for a detailed description of how the differential operators are discretised and the matrices are constructed). Equation (12) is a linear system of ordinary differential equations in time with the streamfunction at the collocation points as unknowns. By erasing the time derivative, the equilibrium state (i.e., the stationary solution) of the linearised system is obtained as

$$\widehat{\psi}_j = A^{-1}\widehat{F} . \tag{13}$$

A question arises now about how the equilibrium state (13) is obtained for an arbitrary infinitesimal perturbation. The solution of (12) can be written as the sum of the homogeneous solution (starting from a given initial condition) plus a forced solution. By introducing the modal ansatz $\widehat{\psi}_j = \overline{\psi}_j e^{-i\omega t}$ it is possible to solve the homogeneous problem as an eigenvalue one,

https://doi.org/10.5194/egusphere-2023-316
Preprint. Discussion started: 13 March 2023

identifying the eigenvalues $\omega \in \mathbb{C}$ and the associated eigenfunctions for each azimuthal wavenumber, m. If all the complex eigenvalues have negative imaginary part the system is stable and it will converge to the equilibrium state (13), while the perturbations will grow with time if at least one eigenvalue has positive imaginary part. The real part of the eigenvalues, on the other hand, is associated with phase propagation in the zonal direction.

The advantage of the proposed framework is that the behaviour of the system is determined from the eigenvalues of the homogeneous problem, that are *independent* of the forcing and have indeed general validity for a given zonal background flow. In particular, the sign of the imaginary part of the eigenvalues determines whether a perturbation will grow or decay. The evolution of a perturbation, be it initiated by the forcing or by a generic initial condition, is obtained as an initial value problem which becomes drastically simplified by means of the modal analysis (as detailed in the appendix). The eigenvalue code has been written in Python, where Chebyshev polynomials have been implemented following Peyret (2002) and Canuto et al. (2006). The linear problem has been discretised into an equal number of latitudes and longitudes without any aliasing consideration or numerical stability constraints.

In order to check the code quality, an independent numerical assessment of the barotropic vorticity equation has been implemented by using the spherical harmonics transform (SHT) package from Schaeffer (2013). Both the linear and nonlinear barotropic vorticity equations were implemented and compared to the results of the proposed linearised framework. A triangular truncation scheme was adopted with an aliasing-removal approach in both the linear and nonlinear simulation with spherical harmonics (although this was necessary only for the latter). A leapfrog scheme was used for the temporal discretization with time step of 10 minutes. A Robert-Asselin filter with filter parameter 0.01 was implemented to eliminate the spurious computational mode associated with the leapfrog method (Kalnay, 2003).

In all simulations, only the dissipative term $-\lambda_r \nabla_h^2 \psi'$ (with $\lambda_r = (7\ \mathrm{d})^{-1}$ as in Wirth, 2020) was used to make the barotropic wave decay and no hyperviscosity term was introduced. The planetary radius was taken as 6371 km while the planetary rotation speed was $\Omega = 7.292115 \cdot 10^{-5}\ \mathrm{rad\,s^{-1}}$.

3 Model validation

The proposed linearised framework based on Chebyshev polynomials (from now on referred to as the linear method) is first compared with the test cases proposed by Wirth (2020) for two of the investigated zonal velocity profiles. Since the topographic forcing F is stationary, the constant forcing solution provided by Eq. (A7) is used. The expression is further simplified here as the initial perturbation streamfunction is assumed to be zero, implying the vanishing of the first term of (A7), so that only the forced response needs to be computed.

Our analysis framework is able to consider any generic zonal velocity profile that satisfies the boundary conditions at the poles. In the special case of solid body zonal velocity profile, $U = \overline{U}\sin\theta = \overline{U}\cos\varphi$, and the linearised homogeneous barotropic vorticity equation (8) reduces to

$$\frac{\partial \nabla_h^2 \psi'}{\partial t} + \overline{U}\frac{\partial \nabla_h^2 \psi'}{\partial \lambda} + 2\left(\overline{U} + \Omega a\right)\frac{\partial \psi'}{\partial \lambda} + \lambda_r \nabla_h^2 \psi' = 0\,. \tag{14}$$

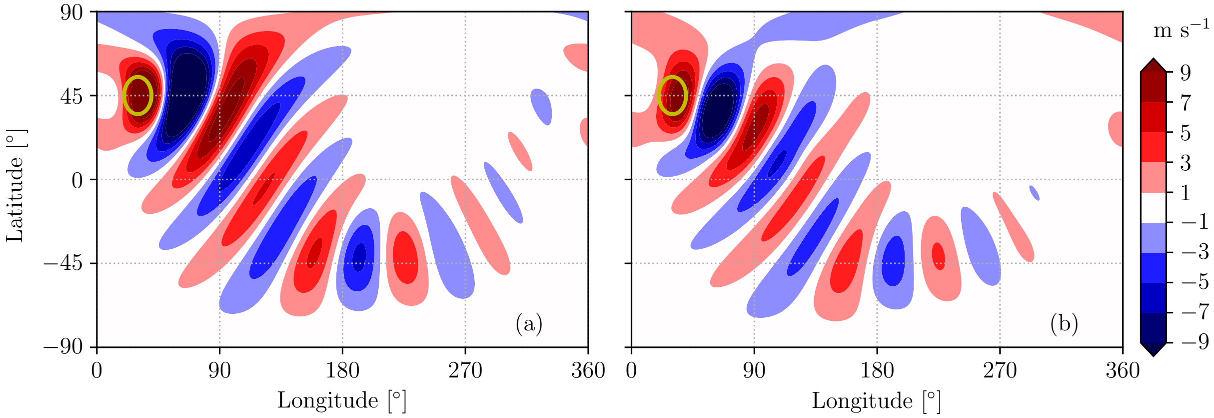

Figure 1. Meridional velocity pattern at the equilibrium state for the zonal velocity profile $U = 15\cos\varphi$ from the linear analysis (a) and after 100 days with the nonlinear solver (b). The circle indicates the topographic forcing.

Equation (14) can be solved analytically by means of the ansatz $\psi' \propto Y_l^m(\theta,\lambda)\,e^{-i\omega t}$ where Y_l^m is the spherical harmonic with degree l and order m. The resulting dispersion relationship is

$$\omega = m\left[\overline{U} - \frac{2\overline{U} + 2\Omega a}{l(1+l)}\right] - i\lambda_r\,, \tag{15}$$

which is a well-known analytical results for Rossby-Haurwitz waves (Haurwitz, 1940). Interestingly, the attenuation parameter λ_r makes the eigenvalue stable, while the first term of (15) is associated with the zonal phase propagation of the wave, similarly to the planar case. From this analysis it is already known that all the modes of the solid-body zonal velocity case are stable (since $\lambda_r > 0$), that the modes are spherical harmonics and that the dispersion relationship is given by (15). Simulations done with different grid resolutions showed an excellent agreement between the analytical relationship (15) and the numerical eigenvalues, with error comparable to the precision of the machine (not shown).

Fig. 1a shows the meridional velocity field (positive northward) and the associated wave pattern at the equilibrium state (13) created by a smooth, idealized mountain located at latitude $\varphi_F = 45°$ N and longitude $\lambda_F = 30°$ and described by

$$F = -7.73\cdot 10^{-9}(\lambda - \lambda_F)\exp\left[-\frac{(\varphi-\varphi_F)^2}{2\sigma_{\varphi,F}^2} - \frac{(\lambda-\lambda_F)^2}{2\sigma_{\lambda,F}^2}\right] h_F\,, \tag{16}$$

where $\sigma_{\varphi,F} = \sigma_{\lambda,F} = 10°$ and $h_F = 0.3$, unless otherwise stated (Wirth, 2020). The zonal background flow is given by $U = 15\cos\varphi\ \mathrm{m\,s^{-1}}$ (or with $\overline{U} = 15\ \mathrm{m\,s^{-1}}$ as above). Fig. 1a should be compared to the nonlinear solution in Fig. 3a of Wirth (2020): despite the opposite sign, the structure of the wave pattern is very similar, although here obtained without any time integration since the solution will in time converge to the steady-state solution because the imaginary part of the eigenvalues is negative. The linear spherical harmonics solution is practically identical to the Chebyshev approach and therefore the results will not be shown here. The nonlinear solver has slight differences from the linear method, such as a more rapid wave attenuation away from the forcing (as visible in Fig. 1b).

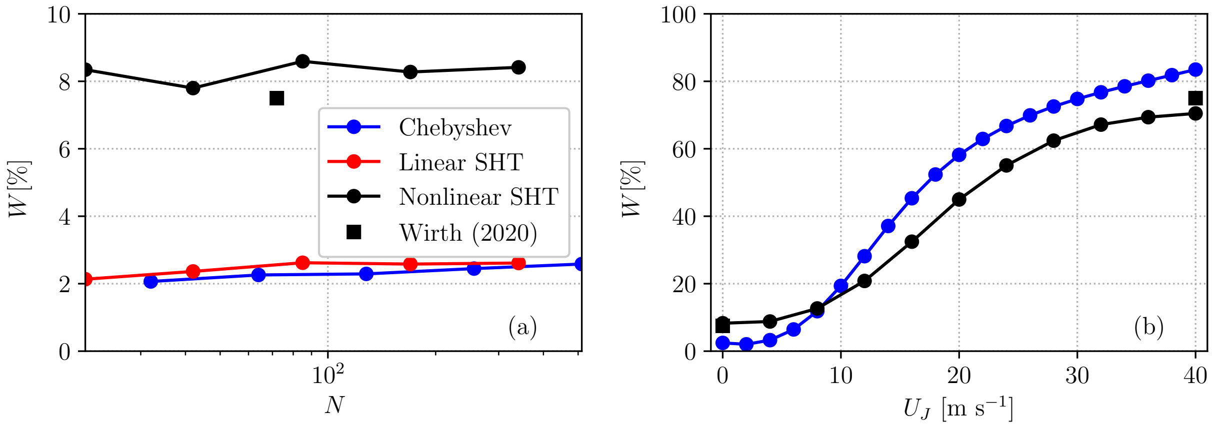

Figure 2. (a) Waveguidability estimated from different linear and nonlinear simulations at different grid resolutions when $U = 15\cos\varphi\,\mathrm{m\,s^{-1}}$ (namely without any latitudinally-confined jet). N for the Chebyshev simulations is given by the number of latitude/longitudes grid points, while for the simulations with the SHT method it is given by the truncation number. (b) Waveguidability assessed for the linear and nonlinear simulations for $N = 256$ (corresponding to a T170 resolution) for different jet velocities U_J (according to the zonal velocity profile given in Eq. 18).

A grid-convergence study can be performed for different grid resolutions. In this study the waveguidability, estimated as in Wirth (2020), has been used as the key quantity for the comparison. The waveguidability of a jet centered around $\varphi = 45°$ N is defined as

$$W = \frac{\int_{\pi/6}^{\pi/3}\cos\varphi\int_{\pi}^{3\pi/2}\mathcal{E}(\varphi,\lambda)\,\mathrm{d}\lambda\,\mathrm{d}\varphi}{\int_{-\pi/2}^{\pi/2}\cos\varphi\int_{\pi}^{3\pi/2}\mathcal{E}(\varphi,\lambda)\,\mathrm{d}\lambda\,\mathrm{d}\varphi}, \tag{17}$$

where $\mathcal{E}(\varphi,\lambda) = \overline{\zeta'^2}/2$ is the enstrophy and the overline indicates the time-average operator performed over the last 90 days of the simulation (after an initial transient time of 10 days), similar to Wirth (2020). Fig. 2a shows the convergence of the waveguidability for different grid resolutions. Noteworthy, convergence of the results is obtained even for moderate resolutions with the linear Chebyshev and linear SHT methods, while the nonlinear method oscillates around a higher value of waveguidability, suggesting once again a difference between linear and nonlinear analyses. The higher value of waveguidability in the nonlinear case is closer to the value reported by Wirth (2020). Having assessed the grid convergence, the rest of the work will use grid resolution $N = 256$ for the Chebyshev computations while a T170 truncation will be used for the SHT method.

4 Single-jet configurations

We will now focus on the case of a latitudinally-confined jet, using the formulation by Wirth (2020)

$$U = \overline{U}\cos\varphi + U_J\exp\left[-\frac{(\varphi-\varphi_J)^2}{2\sigma_J^2}\right] + L(\varphi), \tag{18}$$

where U_J is the jet velocity, $\overline{U} = 15\ \mathrm{m\,s^{-1}}$, $\varphi_J = 45°$ N is the jet latitude and $\sigma_J = 5°$ (unless otherwise stated). L indicates a linear correction that imposes $U(\varphi = \pm\pi/2) = 0$ at the two poles. The waveguidability can be used again to get an integral parameter to compare the linear and nonlinear approaches. Fig. 2b shows how the waveguidability changes for different jet velocities: the two evaluations have the same qualitative trend, although the linear analysis has a sharper transition and achieves a higher final value of waveguidability. The difference between the linear and nonlinear solution must be related to a counterintuitive dissipative effect of the nonlinear terms, neglected in the linear analysis.

4.1 Weak-jet case

Let us consider first a weak-jet case with $U_J = 20\ \mathrm{m\,s^{-1}}$. Fig. 3 shows a comparison between the time evolution of the wave obtained using the linear method and the nonlinear model, as the Gaussian mountain is introduced at $t = 0$. The high resemblance of the two solutions is visible for the first 100 hours and maintained through the length of the simulations, although the meridional wind anomalies in the nonlinear simulation appear slightly weaker and smoother (Fig. 3). Beyond 500 hours both simulations achieve a steady state: this is to be expected, since the linear analysis indicated that all the eigenvalues had negative imaginary part and, thus, the system is stable (see Sec. 2). The result is a stationary wave originated from the interaction of the jet with the topography, featuring both a degree of great-circle and of along-jet propagation.

4.2 Strong-jet case

The strong-jet case with $U_J = 40\ \mathrm{m\,s^{-1}}$ is associated with an unsteady velocity field that, regardless of the integration time, does not achieve a steady state as in the weak-jet case: therefore, after an initial integration time of 10 days, 90 additional days are simulated and time averaged to filter out the transient behaviour (as discussed in Wirth, 2020). The linear analysis indicates that some eigenvalues have positive imaginary part and, therefore, the flow field is unstable according to linear theory. The nonlinear simulation, however, does not display such an unrealistic divergence of wave amplitudes: a great-circle wave propagation is still present as in the solid-body velocity case, but there is also a wave pattern in the zonal direction in the waveguide corresponding to the strong jet. At long simulation times, the behavior is broadly similar as in the weak-jet case at long simulation times (see Fig. 4), but the zonal wavelength is larger; the latter is expected and can be understood with the help of the Rossby wave dispersion relation for stationary conditions.

The linear eigenvalue analysis suggests that the equilibrium state (13) is unstable, so any perturbation should grow exponentially with time. Nevertheless, such an unstable equilibrium state (as obtained from from the linearised barotropic equation) resembles quite closely the time-averaged nonlinear solution, which is bounded and characterised by the averaged field reported in Fig. 4b. Beyond the linearly stable range, only the nonlinear simulations could provide some information about what is actually happening. In order to shed some light, an empirical orthogonal function (EOF) approach has been applied to the nonlinear simulation and the corresponding modes are shown in Fig. 5. The figure indicates that the first mode is practically constant in time and remains close to the time-averaged field of the nonlinear simulation, while the second-third, fourth-fifth, and sixth-seventh modes organize themselves to create traveling wave patterns with zonal wavenumbers respectively $m = 5$, $m = 6$ and $m = 7$, respectively (not shown). These first seven modes contain 60% of the meridional velocity variance. The

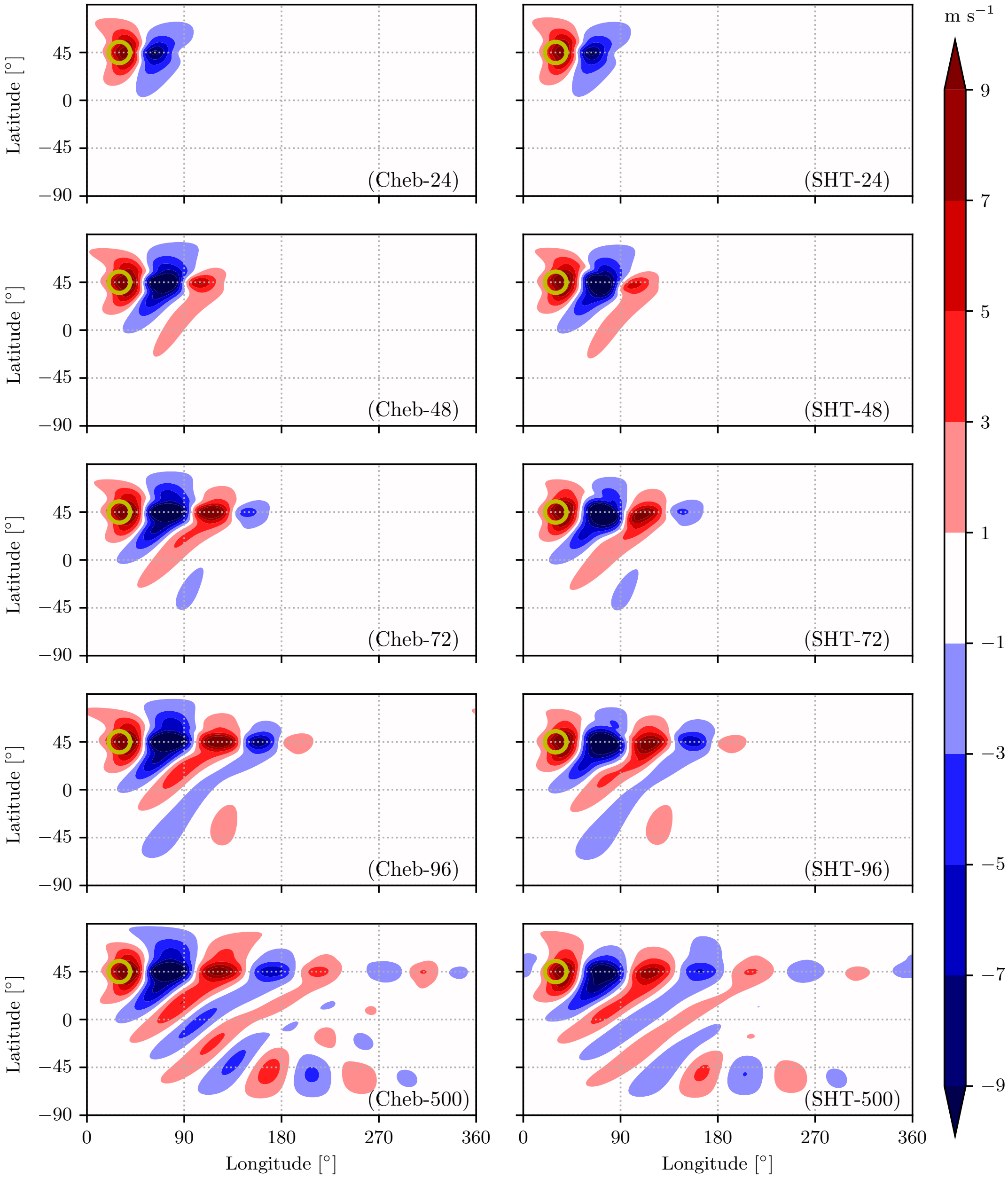

Figure 3. Meridional velocity patterns at different times from the linear analysis (left) and the nonlinear solver (right) for a jet located at $\varphi_J = 45°$ N and $U_J = 20\ \mathrm{m\,s^{-1}}$. The circle indicates the topographic forcing, switched on at $t = 0$ h. The actual time of the simulation (in hours) is indicated in the brackets.

210 modal coefficients of mode 2 and 3 resemble each other, and similarly happens for modes 4 and 5 (the coefficients have been normalised by their root mean square to ensure unitary oscillation amplitude). The trajectories in the plane spanned by the

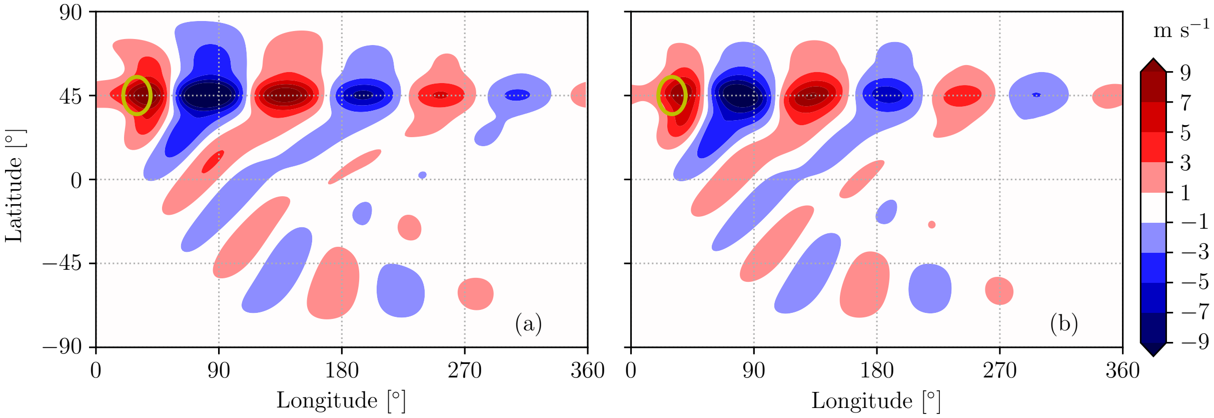

Figure 4. Meridional velocity in the strong-jet case ($U_J = 40\ \mathrm{m\,s^{-1}}$) from the linear method at the equilibrium state (a). Meridional velocity field averaged between 10 and 100 days from the simulation start with the nonlinear solver (b). The circle indicates the topographic forcing.

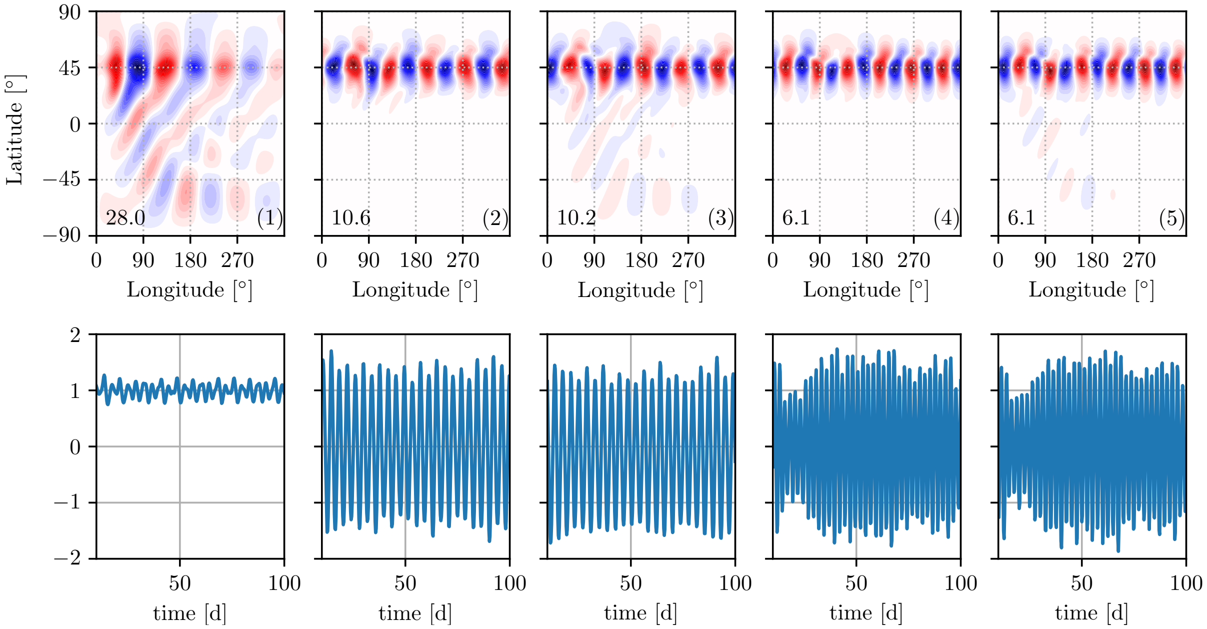

Figure 5. First five modes of the EOF decomposition of the meridional velocity field obtained from the nonlinear simulations (top) and their temporal coefficient normalised by their root mean square value (bottom) for the strong-jet case with $U_J = 40\ \mathrm{m\,s^{-1}}$. The number in the bottom-left corner of the first row indicates the variance contribution of each mode. The modes in the first row have unitary norm and the color scale is not consistent between different modes since each mode has unitary norm.

corresponding modal amplitudes, shown in Fig. 6, belong to a closed orbit, suggesting a limit cycle (in dynamical systems language, Strogatz, 2018). Since a limit cycle is associated with a nonlinearity of the system, a linear analysis cannot identify that,

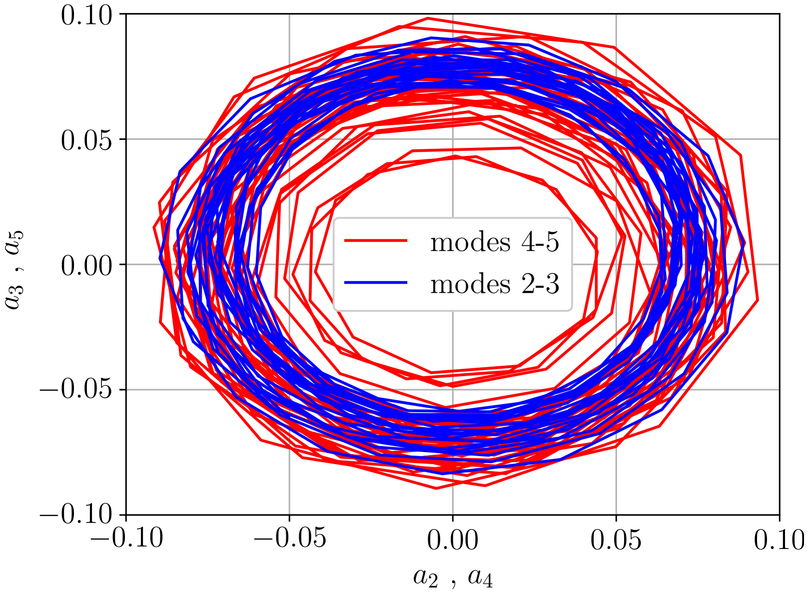

Figure 6. Evolution of the amplitude of mode 2 (4) plotted against the amplitude of mode 3 (5) from the EOF analysis shown in Fig. 5.

and this is consistent with the apparent divergence of the linear solution. The limit cycle orbits around the unstable equilibrium state of the system (provided by the first EOF mode), approximated in its linear version by (13).

Additional simulations where the orographic forcing was moved to lie right on the equator did not change this overall picture, and the traveling waves remained at the jet latitude. This implies that the wave components described by the EOF analysis are traveling waves determined just by the background flow, rather than by the forcing as suggested by the linear analysis. One might wonder if there is a correspondence between the unstable modes of the linear analysis and the most energetic EOF modes. Fig. 4 shows already that the equilibrium state approximates the time average (i.e. the first EOF mode). Fig. 7 shows instead the four most unstable modes of the linear analysis sorted according to their growth rates. Once again the reader is reminded that these modes are obtained from a homogeneous analysis and thus irrespective of the forcing. The linear unstable waves are located at the jet latitude and share many features with the first EOF modes (the phase and amplitude of the linear modes are arbitrary). Despite the similarity, however, the most-rapidly growing mode ($m = 6$, Fig. 7a) does not exactly match the EOF patterns corresponding to the modes 2 and 3 (which appear to project on $m = 5$, cf. Fig. 5). We will further delve on the factors determining the shape of the unstable modes in the next section.

4.3 Stability analysis

A systematic stability analysis can be conducted for different zonal velocity profiles U to identify at which jet velocity perturbations will or will not amplify. Fig. 8 shows the results of such an analysis for a narrow jet ($\sigma_J = 5°$) zonal profile with different U_J values and φ_J (the colatitudes belonging to the southern hemisphere are specular). At low U_J values the imaginary part of the most unstable eigenvalue is determined by the dissipation parameter λ_r but, as U_J increases, the stability margin

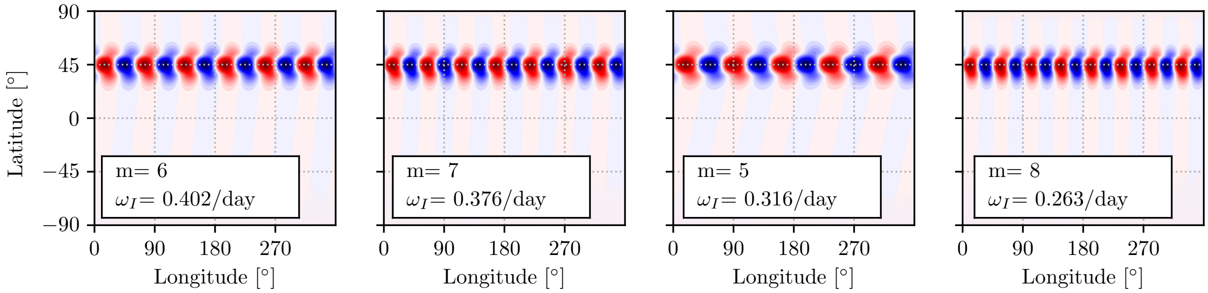

Figure 7. The 4 most unstable modes from the linear analysis sorted according to their growth rate in the strong-jet case.

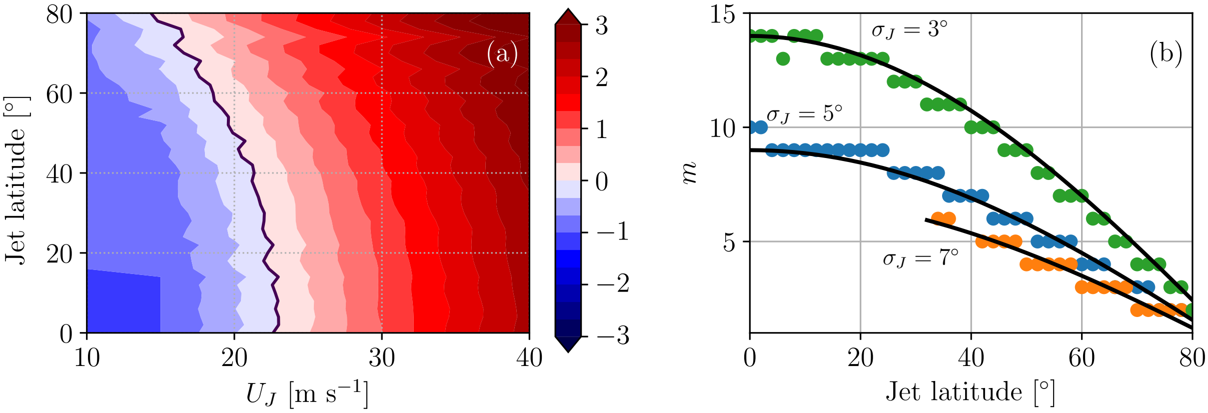

Figure 8. (a) Maximum of the imaginary part of the eigenvalues for a given jet velocity (normalised by λ_r) when $\sigma_J = 5°$. The black line indicates the neutral curve. (b) Azimuthal wavenumber of the most unstable eigenvalue for $U_J = 40\ \mathrm{m\,s^{-1}}$ for different jet widths. The black lines are curves $m \propto \cos\varphi_J$ fitting the linear stability results.

decreases and above 15-22 $\mathrm{m\,s^{-1}}$ at least one eigenvalue becomes unstable. The higher the jet velocity, the higher is the growth rate and this explains why the nonlinear simulation is stable up to a certain jet velocity (around 28 $\mathrm{m\,s^{-1}}$ for $\varphi_J = 45°$ N) and it becomes unstable afterwards. A weaker jet velocity is needed for the instability onset when the jet approaches the pole.

It is also interesting to monitor the wavenumber associated with the most unstable eigenvalue. After the onset of the linear instability, this wavenumber does not depend on U_J, and therefore the maximum growth rate in Fig. 8 is only shown for $U_J = 40\ \mathrm{m\,s^{-1}}$, where the jet is unstable at all latitudes. For $\varphi_J = 45°$ N a wavenumber $m = 6$ is the most unstable, similar to what pointed out by the EOF analysis. However, as the jet is shifted to the pole, the most unstable wavenumber systematically decreases following the cosine of φ_J. It is possible to explain this trend by assuming that the instability is associated with a wavelength independent of the latitude, given by

$$L = \frac{2\pi}{m} a\cos\varphi = \text{constant}\,, \tag{19}$$

which is indeed proportional to $\cos\varphi$. This implies that the most barotropically-unstable Rossby wave has the same wavelength at different latitudes of the zonal jet. Inspired by the analysis of Gill (1982), it is expected that the Rossby wave will become more unstable for narrower jet width, σ_J, and conversely less unstable for a wider jet. Fig. 8b shows the zonal wavenumber of the most unstable mode for $U_J = 40\ \mathrm{m\,s^{-1}}$ and three different jet widths. The very narrow one shows that the wavelength of the most unstable Rossby wave becomes shorter moving towards larger m (but remains still constant in latitude), while the broader one shows the opposite trend and moves towards smaller m. Interestingly, the broader jet (just $\sigma_J = 7°$) is unstable only when the jet is far enough from the equator and it is stable for $\varphi_J < 30°$ N. By having the even higher value $\sigma_J = 10°$, the instability disappears at all jet latitudes and the flow becomes stable again at $U_J = 40\ \mathrm{m\,s^{-1}}$.

5 The double-jet case

After having considered the single-jet case, we now consider a configuration with two separate jets located at different latitudes. Only the narrow jet width $\sigma_J = 5°$ will be considered. The double-jet setup was chosen as it is representative of the interplay between the subtropical and the eddy-driven jet streams observed in the Northern Hemisphere, and because recent research has connected it to the occurrence of quasi-stationary Rossby waves and summer heat extremes (Rousi et al., 2022). The first jet is located at $\varphi_J = 30°$ N and has a jet velocity of $U_J = 40\ \mathrm{m\,s^{-1}}$ (the associated perturbation field is shown in Fig. 9 once again for both the linear and nonlinear simulation). The second jet is located at $\varphi_J = 60°$ N and has also a jet velocity of $U_J = 40\ \mathrm{m\,s^{-1}}$ (the associated perturbation field is shown in Fig. 10).

The perturbations resulting from the 30°N jet feature a combination of great-circle and along-jet propagation, that is properly represented by both the linear and nonlinear approaches (Fig. 9). On the other hand, for the jet at 60° N the along-jet propagation is obtained only in the linear simulation, while it is much weaker in the nonlinear simulation (Fig. 10). The weakening of along-jet propagation can be due to an enhanced equatorward propagation of the stationary wave in the nonlinear case, given that the forcing is located at 45° N, possibly combined with enhanced dissipation.

Moving to the double-jet configuration we notice, first of all, a good agreement between the linear and the nonlinear solution (Fig. 11). Rossby wave propagation occurs separately along the waveguides delineated by the two jet streams, while great-circle propagation to the Southern Hemisphere is smaller in the double-jet configuration than for the jets taken singularly. The double-jet pattern corresponds roughly to the combination of the patterns of the linear solutions for the two individual jets. However, this is not true for the nonlinear solutions, because of the previously discussed lack of Rossby wave propagation along the 60°N jet in the nonlinear single-jet case. It might be that forced meridional velocity perturbations along the 30° N jet stream could provide energy to the jet at 60° N, which would otherwise be attenuated as in the single-jet case (Fig. 11b): however, this hypothesis would need further verification.

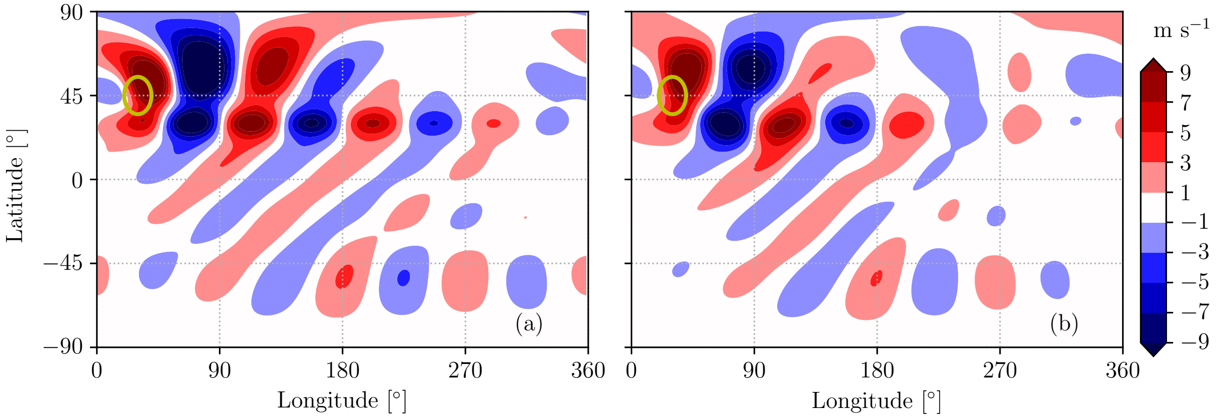

Figure 9. Meridional velocity associated with a zonal jet characterized by $U_J = 40\ \mathrm{m\,s^{-1}}$ with $\varphi_J = 30°$ N at the equilibrium state from the linear analysis (a) and averaged between 10 and 100 days from the simulation start with the nonlinear solver (b).

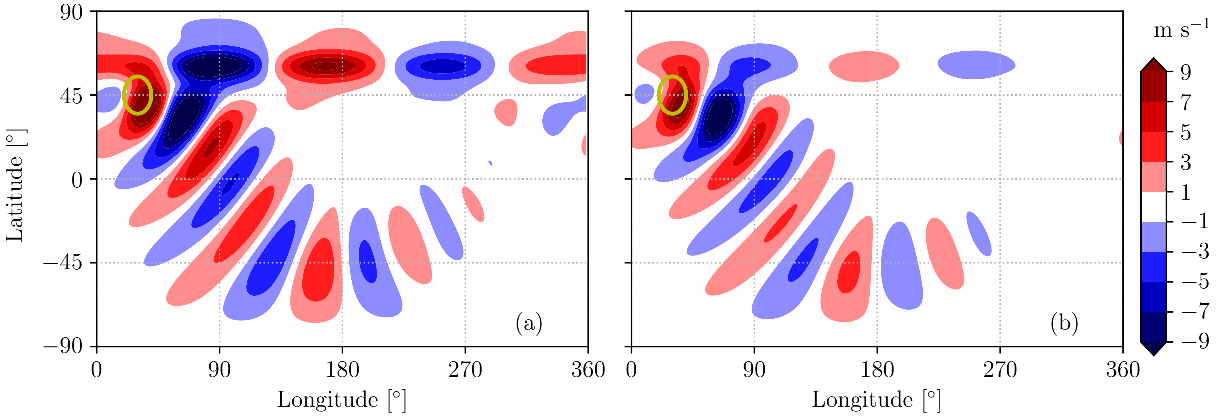

Figure 10. Meridional velocity associated with a zonal jet characterized by $U_J = 40\ \mathrm{m\,s^{-1}}$ with $\varphi_J = 60°$ N at the equilibrium state from the linear analysis (a) and averaged between 10 and 100 days from the simulation start with the nonlinear solver (b).

6 Conclusions

A linearised framework is proposed to solve the barotropic vorticity equation and analytically determine the Rossby wave response to topographic forcing in different background flow configurations. First the homogeneous solution is assessed by introducing a modal assumption in the zonal direction and temporal coordinate. This leads to an eigenvalue problem where the eigenfunctions are the modes in the meridional direction. From the eigenvalues it is possible to assess the mode stability by looking at the sign of the imaginary part (a positive value indicates linear instability and exponential growth of the mode when triggered). The forced case is treated as an initial value problem but the solution is now much facilitated by the modal analysis of the homogeneous equation and no numerical integration nor additional modal analysis is required. If all the modes are stable, the system will approach an equilibrium condition related to the forcing and the background flow field.

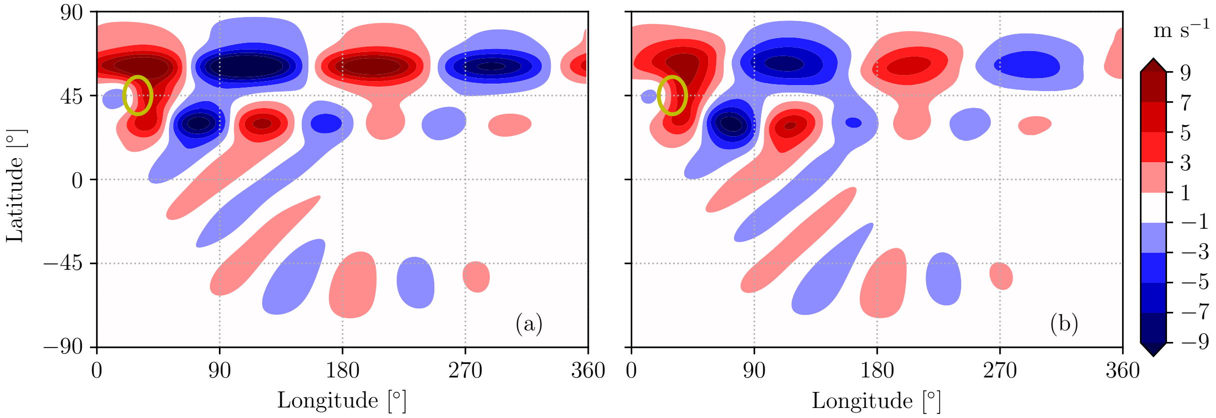

Figure 11. Meridional velocity associated with two zonal jets ($U_{J,1} = 40\,\mathrm{m\,s^{-1}}$ with $\varphi_{J,1} = 30°$ N and $U_{J,2} = 40\,\mathrm{m\,s^{-1}}$ with $\varphi_{J,2} = 60°$ N) at the equilibrium state from the linear analysis (a) and averaged between 10 and 100 days from the simulation start with the nonlinear solver (b).

The proposed linear framework has been compared with nonlinear simulations performed with a spectral code based on spherical harmonics. The analysis of the jet waveguidability showed small quantitative differences between the linearised solution and the nonlinear simulations. Strong-jet cases, characterised by unstable eigenvalues, showed a different behaviour from the expected divergence of the linear solution: the flow field did not diverge exponentially, instead oscillating around an unstable equilibrium state. This dynamics was further investigated by means of empirical orthogonal functions, showing that modes with an azimuthal wavenumber of 5 up to 7 are associated with traveling waves and a limit cycle, a dynamics driven by nonlinear effects. Nevertheless, the averaged flow field in the nonlinear simulation resembles (equally well as for other stable cases) the unstable equilibrium state calculated from the linear method: this is an equilibrium state obtained by removing the time derivative and is therefore an approximation of the equilibrium condition of the nonlinear system too. This consideration is not just restricted to the center of the limit cycle (i.e. the mean of the atmospheric state), but also to the other modes of the EOF: this was verified by comparing higher EOF modes with the unstable modes from the linear analysis, and the two showed good resemblance.

Another point of interest came from the linear stability analysis. For a jet placed at a latitude of 45° N, the linear method estimated a transition from stable to unstable at around $U_J \approx 20\ \mathrm{m\,s^{-1}}$, beyond which a limit cycle should be observed. However, the nonlinear simulations actually achieved a stationary state at large time (namely without any limit cycle) up to $U_J \approx 28\ \mathrm{m\,s^{-1}}$, beyond which a limit cycle was established. We hypothesize that this transition delay is associated with the role of nonlinear terms as stabilizing elements. This was also observed from the spatial distribution of the wave that appeared always smoother in the nonlinear simulations compared to the linear approach (ruling out possible differences in the numerical diffusion). This transition delay could be investigated using nonlinear stability methods to reveal wave-wave interactions and the role of nonlinear terms in the instability onset, although this has not been attempted in the present work. It seems clear however that linear instability is necessary to observe the emergence of nonlinear instability, but not sufficient.

https://doi.org/10.5194/egusphere-2023-316
Preprint. Discussion started: 13 March 2023

The stability analysis also allowed to estimate the preferred azimuthal wavenumber of the moving Rossby wave train associated with the barotropic instability. The wavenumber decreases with jet latitude and is only weakly dependent on the jet intensity. A high sensitivity of the preferred azimuthal mode and of the instability onset was instead observed for different jet widths: very narrow jet widths promote higher growth rates and shorter wavelengths, in agreement with the link between vorticity gradients and instability.

The application of the proposed approach to a double-jet configuration indicates that: a) the equatorward propagation of Rossby waves is weakened in a double-jet case; and b) the double-jet response roughly corresponds to the linear combination of the individual jet responses. However, the possibility of an interaction between the wave trains associated with the two jets cannot be not ruled out, especially if the two are not located sufficiently far apart. We stress that these conclusions about double-jet configurations should be regarded as preliminary undertakings on the matter, and they need to be backed up by the comprehensive analysis of several background flow and forcing configurations.

In conclusion, we believe that the proposed method is a relatively simple and computationally efficient way to study the steady and unsteady Rossby wave response to topography in a variety of idealized background flow configurations. This study should be regarded as an introduction and explanation of the techniques, but possible applications of this approach could include systematic waveguidability assessments for different forcings and background zonal wind profiles. A relevant application of this approach would be to understand the role of orography in forcing Rossby waves with specific zonal wavenumbers, which appear to get amplified and involved in surface weather extremes during summer (as noticed, among others, by Jiménez-Esteve et al., 2022).

Appendix A: Spectral solution of the barotropic vorticity equation

Equation (11) introduces the Laplace operator $\mathcal{L}$ in the transformed space together with the boundary conditions needed to avoid the pole singularity

$$\widehat{\psi}(\theta=0)=0 \qquad \text{for} \qquad m\neq 0 \qquad \text{and} \qquad \left.\frac{\partial\widehat{\psi}}{\partial\theta}\right|_{\theta=0}=0 \qquad \text{for} \qquad m\neq\pm1, \tag{A1}$$

and similarly for $\theta=\pi$. Consequently, there are two boundary conditions for $|m|\leq 1$ and four otherwise. An additional boundary condition must be introduced at $m=0$ as $\widehat{\psi}(\theta=0)=0$ in order to set the value of the streamfunction at one pole since, otherwise, the streamfunction would be defined up to an additive constant, making the numerical problem singular.

Following Peyret (2002), the solution of (10) is calculated by a spectral collocation method in terms of orthogonal polynomials. In the present work, Chebyshev polynomials, $T_q(\theta)$, and the decomposition

$$\widehat{\psi}(\theta,t;m)\approx\sum_{q=0}^{N}a_q(t;m)\,T_q(\theta)\,, \tag{A2}$$

https://doi.org/10.5194/egusphere-2023-316
Preprint. Discussion started: 13 March 2023

are used since the transform process is analytic. The $N+1$ collocation points are described by a shifted Gauss-Lobatto distribution

$$\theta_j = \frac{\pi}{2}\left[1-\cos\left(\pi\frac{j}{N}\right)\right] \qquad \text{with} \qquad j\in\{0,1,\dots,N-1,N\}\,, \tag{A3}$$

implying a refinement of the colatitude distribution near the poles. This is in contrast with the Legendre and associated Legendre polynomials that account for a more appropriate resolution at the poles. Nevertheless, Chebyshev polynomials have been preferred here since an exact method to calculate the spectral coefficients exists for them, while the Legendre polynomials require a numerical quadrature scheme (Krishnamurti et al., 2006).

Rather than working with the spectral coefficients, $a_q(t;m)$, here it is preferred to work directly with the value of the streamfunction at the collocation points, $\widehat{\psi}_j = \widehat{\psi}(\theta_j,t;m)$, as unknowns collected to a vector, significantly facilitating the interpretation of the results. The derivatives of the streamfunction are calculated as

$$\left.\frac{\partial\widehat{\psi}}{\partial\theta}\right|_j \approx D^{(1)}\widehat{\psi}_j \qquad , \qquad \left.\frac{\partial^2\widehat{\psi}}{\partial\theta^2}\right|_j \approx D^{(2)}\widehat{\psi}_j\,, \tag{A4}$$

where the matrices $D^{(1)}$ and $D^{(2)}$ provide the first- and second-order derivatives (Peyret, 2002). Another advantage of the Chebyshev basis is that the matrices $D^{(1)}$ and $D^{(2)}$ are analytically known (Peyret, 2002; Canuto et al., 2006), although some modifications to limit the effect of round-off errors have been implemented (Bayliss et al., 1995).

By exploiting (A4), the discretised Laplace operator becomes

$$\mathcal{L} \approx D^{(2)} + \cot\theta\, D^{(1)} - \frac{m^2}{\sin^2\theta} I\,, \tag{A5}$$

where I indicates the identity matrix. This implies that the Laplace operator becomes a numerical matrix since the spatial dependence of the variables is provided by the Fourier modes (in the zonal direction) and by the Chebyshev polynomials (in the meridional direction). Once the Laplace operator has been discretised, the matrices A and B in equation (12) are obtained from their definition.

As stated in (A1), the boundary conditions at the poles have been imposed by removing 2, 3 or 4 points from the analysis so that the size of the matrices A or B is $N-2\times N-2$ for $m=0$, $N-1\times N-1$ for $|m|=1$ and $N-3\times N-3$ otherwise. This has the advantage that the reduced forms of A and B are just related to the dynamics of the modeled system rather than the boundary conditions (the reader is referred to section 3.7.1 of Peyret, 2002, for a detailed description on how the matrices can be reduced), together with a decrease of the computational cost.

If B is nonsingular, it is possible to perform the eigendecomposition $B^{-1}A = P\Lambda P^{-1}$ where the columns of P are the eigenvectors and Λ is a diagonal eigenvalue matrix. The analytical solution of (12) is found to be

$$\widehat{\psi}_j(t;m) = Pe^{-i\Lambda t}\left[P^{-1}\widehat{\psi}_j(0;m) + i\int\limits_0^t e^{i\Lambda\tau}P^{-1}B^{-1}\widehat{F}(\tau)\,\mathrm{d}\tau\right]\,, \tag{A6}$$

with $\widehat{\psi}_j(0;m)$ indicating the initial condition of the streamfunction. In the special case of a steady forcing, (A6) becomes

$$\widehat{\psi}_j(t;m) = Pe^{-i\Lambda t}P^{-1}\widehat{\psi}_j(0;m) + \left(I - Pe^{-i\Lambda t}P^{-1}\right)A^{-1}\widehat{F}\,. \tag{A7}$$

The first term of (A6) and (A7) is the homogeneous unforced solution of the linear system with initial condition $\widehat{\psi}_j(0;m)$, while the second term is the forced solution with zero initial condition.

Since the eigenvalues Λ and eigenfunctions P depend on the zonal velocity U, Rossby number, Ro, and wavenumber, m, they are calculated and stored for all the considered wavenumbers for a given zonal velocity profile and Rossby number. Since they do not depend on the actual forcing applied, once they are computed they can be used with any kind of forcing according to (A6-A7). Furthermore, since the equation is linear, no aliasing instability is present and each eigenmode does not interact with the others.

Author contributions. AS developed the theory, performed the simulations shown in the manuscript and analyzed the data. All authors contributed equally to the interpretation of the results. AS and JR prepared the manuscript, assisted by GM and VW for review and editing.

Competing interests. The authors declare that no competing interests are present.

References

Ambrizzi, T., Hoskins, B. J., and Hsu, H.-H.: Rossby Wave Propagation and Teleconnection Patterns in the Austral Winter, J. Atmos. Sci., 52, 3661–3672, https://doi.org/10.1175/1520-0469(1995)052<3661:RWPATP>2.0.CO;2, 1995.

Baldauf, M. and Brdar, S.: An analytic solution for linear gravity waves in a channel as a test for numerical models using the non-hydrostatic, compressible Euler equations, Quart. J. Roy. Meteor. Soc., 139, 1977–1989, https://doi.org/https://doi.org/10.1002/qj.2105, 2013.

Bayliss, A., Class, A., and Matkowsky, B. J.: Roundoff error in computing derivatives using the Chebyshev differentiation matrix, Journal of Computational Physics, 116, 380–383, 1995.

Boyd, J. P.: The Effects of Latitudinal Shear on Equatorial Waves. Past I: Theory and Methods, J. Atmos. Sci., 35, 2236–2258, https://doi.org/10.1175/1520-0469(1978)035<2236:TEOLSO>2.0.CO;2, 1978.

Branstator, G.: Circumglobal teleconnections, the jet stream Waveguide, and the North Atlantic Oscillation, J. Climate, 15, 1893–1910, https://doi.org/10.1175/1520-0442(2002)015<1893:CTTJSW>2.0.CO;2, 2002.

Campbell, L. and Maslowe, S.: Forced Rossby wave packets in barotropic shear flows with critical layers, Dynamics of Atmospheres and Oceans, 28, 9–37, https://doi.org/https://doi.org/10.1016/S0377-0265(98)00044-X, 1998.

Canuto, C., Hussaini, M. Y., Quarteroni, A., and Zang, T. A.: Spectral methods. Fundamentals in single domains., Sci. Comput., Berlin: Springer, https://doi.org/10.1007/978-3-540-30726-6, 2006.

Coumou, D., Petoukhov, V., Rahmstorf, S., Petri, S., and Schellnhuber, H. J.: Quasi-resonant circulation regimes and hemispheric synchronization of extreme weather in boreal summer, Proc. Nat. Academy Sci., 111, 12 331–12 336, https://doi.org/10.1073/pnas.1412797111, 2014.

Davies, H.: Weather chains during the 2013/2014 winter and their significance for seasonal prediction, Nature Geosci., 8, 833–837, https://doi.org/10.1038/ngeo2561, 2015.

Di Capua, G., Sparrow, S., Kornhuber, K., Rousi, E., Osprey, S., Wallom, D., van den Hurk, B., and Coumou, D.: Drivers behind the summer 2010 wave train leading to Russian heatwave and Pakistan flooding, npj Climate and Atmospheric Science, 4, 1–14, 2021.

Fragkoulidis, G., V., W., P., B., and H., F. A.: Linking Northern Hemisphere temperature extremes to Rossby wave packets, Quart. J. Roy. Meteor. Soc., 144, 553–566, https://doi.org/10.1002/qj.3228, 2018.

Gill, A. E.: Atmosphere-ocean dynamics, vol. 30, Academic press, 1982.

Harnik, N., Messori, G., Caballero, R., and Feldstein, S. B.: The Circumglobal North American wave pattern and its relation to cold events in eastern North America, Geophys. Res. Lett., 43, 11,015–11,023, https://doi.org/https://doi.org/10.1002/2016GL070760, 2016.

Haurwitz, B.: The motion of atmospheric disturbances on the spherical earth, J. mar. Res, 3, 254–267, 1940.

Held, I. M., Ting, M., and Wang, H.: Northern Winter Stationary Waves: Theory and Modeling, J. Climate, 15, 2125–2144, https://doi.org/10.1175/1520-0442(2002)015<2125:NWSWTA>2.0.CO;2, 2002.

Hoskins, B. and Woollings, T.: Persistent Extratropical Regimes and Climate Extremes, Curr. Climate Change Rep., 1, 115–124, https://doi.org/10.1007/s40641-015-0020-8, 2015.

Hoskins, B. J. and Karoly, D. J.: The steady linear response of a spherical atmosphere to thermal and orographic Forcing, J. Atmos. Sci., 38, 1179–1196, https://doi.org/10.1175/1520-0469(1981)038<1179:TSLROA>2.0.CO;2, 1981.

Hoskins, B. J. and Valdes, P. J.: On the existence of Storm-Tracks, J. Atmos. Sci., 47, 1854–1864, https://doi.org/10.1175/1520-0469(1990)047<1854:OTEOST>2.0.CO;2, 1990.

https://doi.org/10.5194/egusphere-2023-316
Preprint. Discussion started: 13 March 2023

Jiménez-Esteve, B., Kornhuber, K., and Domeisen, D. I. V.: Heat Extremes Driven by Amplification of Phase-Locked Circumglobal Waves Forced by Topography in an Idealized Atmospheric Model, Geophys. Res. Lett., 49, e2021GL096 337, https://doi.org/10.1029/2021GL096337, 2022.

Kalnay, E.: Atmospheric modeling, data assimilation and predictability, Cambridge university press, 2003.

Kornhuber, K., Petoukhov, V., Petri, S., Rahmstorf, S., and Coumou, D.: Evidence for wave resonance as a key mechanism for generating high–amplitude quasi–stationary waves in boreal summer, Clim. Dyn., 49, 1961–1979, https://doi.org/10.1007/s00382-016-3399-6, 2017.

Kornhuber, K., Osprey, S., Coumou, D., Petri, S., Petoukhov, V., Rahmstorf, S., and Gray, L.: Extreme weather events in early summer 2018 connected by a recurrent hemispheric wave-7 pattern, Environ. Res. Lett., 14, 054 002, https://doi.org/10.1088/1748-9326/ab13bf, 2019.

Krishnamurti, T. N., Bedi, H., Hardiker, V., and Watson-Ramaswamy, L.: An introduction to global spectral modeling, vol. 35, Springer Science & Business Media, 2006.

Manola, I., Selten, F., de Vries, H., and Hazeleger, W.: "Waveguidability" of idealized jets, J. Geophys. Res.: Atmospheres, 118, 10,432–10,440, https://doi.org/10.1002/jgrd.50758, 2013.

Martius, O., Schwierz, C., and Davies, H. C.: Tropopause-Level Waveguides, J. Atmos. Sci., 67, 866–879, https://doi.org/10.1175/2009JAS2995.1, 2010.

Petoukhov, V., Rahmstorf, S., Petri, S., and Schellnhuber, H. J.: Quasiresonant amplification of planetary waves and recent Northern Hemisphere weather extremes, Proc. Nat. Acad. Sci., 110, 5336–5341, https://doi.org/10.1073/pnas.1222000110, 2013.

Petoukhov, V., Petri, S., Kornhuber, K., Thonicke, K., Coumou, D., and Schellnhuber, H. J.: Alberta wildfire 2016: Apt contribution from anomalous planetary wave dynamics, Sci. Rep., 8, 12 375, https://doi.org/doi.org/10.1038/s41598-018-30812-z, 2016.

Peyret, R.: Spectral methods for incompressible viscous flow, vol. 148, New York, NY: Springer, 2002.

Riboldi, J., Rousi, E., D'Andrea, F., Rivière, G., and Lott, F.: Circumglobal Rossby wave patterns during boreal winter highlighted by space–time spectral analysis, Wea. Clim. Dynamics, 3, 449–469, https://doi.org/10.5194/wcd-3-449-2022, 2022.

Rossby, C.-G.: Relation between variations in the intensity of the zonal circulation of the atmosphere and the displacements of the semi-permanent centers of action, J. Marine Res., 2, 38–55, 1939.

Rossby, C.-G.: Planetary flow patterns in the atmosphere, Quart. J. Roy. Meteor. Soc., 66, 68–87, 1940.

Rousi, E., Kornhuber, K., Beobide-Arsuaga, G., Luo, F., and Coumou, D.: Accelerated western European heatwave trends linked to more-persistent double jets over Eurasia, Nature communications, 13, 1–11, 2022.

Schaeffer, N.: Efficient spherical harmonic transforms aimed at pseudospectral numerical simulations, Geochemistry, Geophysics, Geosystems, 14, 751–758, https://doi.org/10.1002/ggge.20071, 2013.

Stadtherr, L., Coumou, D., Petoukhov, V., Petri, S., and Rahmstorf, S.: Record Balkan floods of 2014 linked to planetary wave resonance, Sci. Adv., 2, e1501 428, 2016.

Strogatz, S. H.: Nonlinear dynamics and chaos: with applications to physics, biology, chemistry, and engineering, CRC press, 2018.

Teng, H. and Branstator, G.: Amplification of waveguide teleconnections in the Boreal summer, Curr. Clim. Change Rep., 5, 421–432, https://doi.org/doi.org/10.1007/s40641-019-00150-x, 2019.

White, R. H., Kornhuber, K., Martius, O., and Wirth, V.: From atmospheric waves to heatwaves: A waveguide perspective for understanding and predicting concurrent, persistent and extreme extratropical weather, Bull. Amer. Meteor. Soc., 103, E923–E935, https://doi.org/10.1175/BAMS-D-21-0170.1, 2022.

Wirth, V.: Waveguidability of idealized midlatitude jets and the limitations of ray tracing theory, Weather Clim. Dynam., 1, 111–125, https://doi.org/10.5194/wcd-1-111-2020, 2020.

Wirth, V. and Polster, C.: The problem of diagnosing jet waveguidability in the presence of large-amplitude eddies, J. Atmos. Sci.", pp. 3137–3151, https://doi.org/10.1175/JAS-D-20-0292.1, 2021.

445 Wirth, V., Riemer, M., Chang, E. K. M., and Martius, O.: Rossby wave packets on the midlatitude waveguide – A review, Mon. Wea. Rev., 146, 1965–2001, https://doi.org/10.1175/MWR-D-16-0483.1, 2018.